Active liquid crystals powered by force-sensing DNA-motor clusters.

Alexandra M. Tayar[1], Michael F. Hagan[2], Zvonimir Dogic[1,2*]

[1]Department of Physics, University of California, Santa Barbara, CA, USA.
[2]Department of Physics, Brandeis University, Waltham, MA, USA.

The authors declare no conflict of interest
*Corresponding author: zdogic@physics.ucsb.edu

Keywords: active matter | liquid crystals | molecular motors | DNA force sensor

Abstract: Cytoskeletal active nematics exhibit striking non-equilibrium dynamics that are powered by energy-consuming molecular motors. To gain insight into the structure and mechanics of these materials, we design programmable clusters in which kinesin motors are linked by a double-stranded DNA linker. The efficiency by which DNA-based clusters power active nematics depends on both the stepping dynamics of the kinesin motors and the chemical structure of the polymeric linker. Fluorescence anisotropy measurements reveal that the motor clusters, like filamentous microtubules, exhibit local nematic order. The properties of the DNA linker enable the design of force-sensing clusters. When the load across the linker exceeds a critical threshold the clusters fall apart, ceasing to generate active stresses and slowing the system dynamics. Fluorescence readout reveals the fraction of bound clusters that generate interfilament sliding. In turn, this yields the average load experienced by the kinesin motors as they step along the microtubules. DNA-motor clusters provide a foundation for understanding the molecular mechanism by which nanoscale molecular motors collectively generate mesoscopic active stresses, which in turn power macroscale non-equilibrium dynamics of active nematics.

Significance statement: Single-molecule techniques have elucidated how isolated molecular motors generate piconewton forces with unprecedented detail. However, in diverse biological and synthetic settings, force generating proteins collectively power non-equilibrium dynamics, including continuous large-scale rearrangements and persistent fluid flows. Characterizing motor-generated forces in these dense and dynamical environments remains a challenge. We assembled a reversible DNA-based force-sensing probe that, by an optical readout, reveals the molecular arrangements and the force loads experienced by kinesin motors. These probes provide insight into motor-generated forces that collectively power the unique dynamics of microtubule-based active nematics, a noteworthy example of an internally-driven active matter system. DNA-based force

probes can be extended to study forces and stresses in various synthetic systems as well as diverse cellular environments.

Main text:

Introduction: Active matter is composed of animate energy-consuming elements that collectively drive the system away from equilibrium, thus endowing it with life-like properties, such as motility and spontaneous flows (1). To make progress towards long-term applications of active matter, it is essential to elucidate the design principles for engineering large scale behaviors by controlling the dynamics of the microscopic constituents. Developing theoretical frameworks have the potential to describe diverse active matter systems, ranging from simple phase-separating colloidal swimmers to complex self-organized mitotic spindles (2–6). Importantly, many active matter systems have anisotropic constituents; thus, their theoretical description needs to account for the local orientational order (7, 8). In such materials, the locally aligned microscopic constituents generate internal active stresses, which in turn drive large-scale chaotic dynamics that includes autonomous flows and creation and annihilation of motile topological defects (9–16). An impactful class of active anisotropic fluids is based on reconstituted cytoskeletal elements, wherein the active stresses are generated by clusters of molecular motors that step along multiple filaments, driving their relative sliding (17, 18). So far, the focus has been on quantifying the chaotic dynamics of cytoskeletal active matter in both the nematic and isotropic phases, and methods of controlling their autonomous flows through boundaries and confinement (19–26). However, being reconstituted from well-defined biochemical components, these systems provide a unique, yet so far largely unexplored, opportunity to elucidate the microscopic origins of the emergent chaotic dynamics, thus paving the way for developing predictive multiscale models (27–29).

The key prerequisite for advancing this line of inquiry is the measurement of active stresses, as these are the primary generators of the non-equilibrium dynamics. This objective requires characterizing the force loads experienced by the molecular motors as they move in dense active nematic environments. Notably, there is a lack of studies in this direction, despite the force load being an essential determinant of motor stepping dynamics (30, 31). The challenge of characterizing these forces in active nematics is compounded by the fact that the motor clusters are advected by the rapid autonomous flows. Thus, measuring motor loads requires Lagrangian force sensors that move with the material. In contrast, most single-molecule techniques such as optical tweezers or atomic force microscopes work in the Eulerian coordinates, where the measurement spring is held fixed in the laboratory reference frame (32).

To address these critical questions, we take advantage of recent advances in DNA-nanotechnology that developed probes for quantifying forces in diverse biological processes, such as cell-matrix interactions, force-induced protein binding, and protein folding. DNA-based probes can be readily integrated into dynamical systems to report locally generated forces with a fluorescent reporter (33–37). Motivated by these results, we integrated DNA-based force-sensing kinesin clusters into microtubule-based active nematics. These clusters have a programmable binding strength, rupturing above critical applied stress, and thereafter ceasing to generate microtubule sliding and associated active stresses. Monitoring the fraction of bound clusters within an active nematic uncovers the average load experienced by the motors, an essential yet previously inaccessible parameter. With a few notable exceptions (38), so far almost all cytoskeletal active matter has been driven by irreversibly linked motor clusters. Programable DNA-based force-sensing motor clusters provide insights into both the molecular structure, mechanics, and active stress generation of microtubule-based active nematics.

Results

Microtubule-based active nematics driven by DNA-kinesin clusters: Conventional active nematics are assembled from stabilized microtubules (MTs), a non-absorbing depletant poly(ethylene glycol) (PEG), and streptavidin clusters of kinesin motors (17, 39). When sedimented on a surfactant-stabilized oil-water interface, the MTs form aligned nematics that are driven away from equilibrium by the motor clusters that convert energy from ATP hydrolysis into interfilament sliding motion. In conventional microtubule-based active matter, active stresses are generated by clusters of tetrameric streptavidin that binds together multiple biotin-labelled processive kinesin-1 motors with an exceedingly strong noncovalent bond.

To understand the mechanism of force generation, we assembled clusters in which two motors are linked by a hybridized double-stranded (ds) DNA (Fig. 1a; SI Appendix, Fig. S1). Single-strands of DNA were modified at their 5’-ends with benzoguanine (BG), which formed a covalent bond with a SNAP-tag fused to the kinesin motor neck (40). DNA linker was formed from two complementary DNA oligos where the hybridized region ranged from 3 to 200 bp. Well-studied properties of DNA allow for the rational design of clusters whose motors were linked by a polymer of known length and elastic compliance. Furthermore, controlling the structure of the hybridized region yielded clusters that rupture above a critical pre-programed force. To understand the influence of the motor-stepping dynamics, we assembled clusters with two different kinesin motors

(Fig. 1a, 1b). First, we used processive double-headed dimeric kinesin-1 motors. Two-headed kinesin takes about 100 consecutive 8 nm steps, before unbinding from a microtubule. At saturating ATP, each step takes ~10 ms (41). Second, we also assembled clusters of non-processive single-headed kinesin-1 motors. In contrast to processive kinesin, a single-headed motor attaches to a MT, takes a single step, and detaches (42–44).

We visualized active nematics by imaging either fluorescent MTs or the fluorescently labelled DNA clusters (Fig. 1c; SI Appendix, Fig. S2). DNA-based clusters bind to neighboring microtubules. As they move towards MT plus ends kinesin motors generate interfilament sliding motion, which in turn generates large-scale chaotic flows. These flows are measured by embedding and tracking micron-sized passive tracer particles. Importantly, the samples exhibited a constant velocity for the duration of the experiment, and a spatially homogenous motor distribution (Fig. 1f). While processive and non-processive kinesins have markedly different single-molecule dynamics, they generated nearly identical collective behavior. We first examined the structural features of active nematics, before using the properties of DNA clusters to gain insight into mechanical forces experienced by motor clusters.

Nematic order of DNA motor clusters: Active nematics are characterized by the local orientational order of their MTs (Fig. 1c). In comparison, little is known about the alignment of motor clusters that generate the active stress. These could have an orientational order that ranges from nearly isotopic to perfectly aligned, and their alignment will impact the efficiency by which they generate dipolar extensile stresses. To gain insight into cluster orientations, we used fluorescence anisotropy measurements to estimate the orientation of the DNA linker. The intercalating fluorophores predominantly absorb and emit polarized light along their transition dipole moment. For the YOYO-1 fluorescent marker, this dipole is perpendicular to the DNA's long axis (45). We excited the DNA-clusters within the nematic film using polarized light, and measured the fluorescent signal that passed through an analyzer that was colinear with the incoming polarized light (Fig. 2a). Fluorescence anisotropy images showed a significant correlation between the local fluorescent intensity and the local MT orientation (Fig. 2b). In comparison, active nematics imaged with unpolarized light yielded a spatially uniform signal.

To estimate the nematic order of the DNA-clusters, we define ϕ as the angle between the DNA's long axis and the colinear polarizer/analyzer (P/A) (Fig. 2a). The emitted fluorescence along the

P/A axis, $I_{||}$, is related to the excitation intensity I, as follows: $I_{||} = I \cdot \cos^2(90^0 - \phi)$. The phase shift is due to the fluorophore's dipole being perpendicular to the DNA's long axis. When $\phi = 90^0$, the dipole is parallel to the P/A axis, yielding a maximal signal. MT-based active nematics yielded maximum fluorescence when MTs were perpendicular to the P/A axis ($\phi = 90^0$), demonstrating nematic order of the DNA clusters, which are on average aligned along the microtubule axis. However, the alignment is far from perfect, as we still measure significant intensity when $\phi = 0^0$. We plot the fluorescence signal as a function of the local MT orientation with respect to the P/A axis, which is equal to the DNA alignment, ϕ (Fig. 2c). We assume that DNA-clusters locally have a Gaussian orientational distribution: $p(\phi) \propto e^{\frac{-(\phi - 90^0)^2}{2\theta^2}}$, were θ^2 is the variance. The measured fluorescent signal is given by: $I_{||} = \sum p(\phi) \cdot \cos^2(\phi - 90)$, where $p(\phi)$ is the fraction of motors pointing along ϕ, and $\cos^2(\phi - 90)$ is the projection on the P/A axis. Using the variance as an adjustable parameter, we fitted the model predictions to experiments (Fig. 2c). The extracted variance is statistically different for different cluster types (SI Appendix, Fig. S3). Subsequently, we used the fitted variance to estimate the nematic order parameter of the rod-like linker: $S = \langle \frac{3}{2}\cos^2\phi - \frac{1}{2} \rangle$. Long-linker clusters of processive motors (200 bp) yielded $S = 0.339 \pm 0.016$, while shorter ones (16 bp) had $S = 0.444 \pm 0.052$. In comparison, clusters with non-processive motors had an even higher order parameter of $S = 0.484 \pm 0.068$.

Very little is known about the microscopic structure of active nematics and how motors are arranged within a microtubule bundles, which makes it difficult to rigorously interpret the measurements of the order parameters. We found lower order for the long DNA clusters. Such clusters allow for a wider range of crosslinking conformation which could cause a wider distribution compared to short DNA. In active nematics, MTs have an almost perfect local alignment. Fluorescence anisotropy results suggest that kinesin clusters have significantly lower nematic order. Some caution is required when interpreting the fluorescence anisotropy experiments. In principle, there could be two distinct populations of motor clusters: one including the force-generating clusters with both motors attached to MTs, and the other including clusters with only a single bound motor. It is possible that the nematic order of the non-force-generating clusters is more isotropic than the doubly-bound clusters. Such bimodal distributions are not accurately described by the assumed Gaussian distribution. In this case, the measured signal, $I_{||}$,

would overestimate the fraction of clusters that have a wider orientation. Thus our analysis provides a lower bound estimate of the nematic order parameter for doubly linked clusters.

DNA binding interactions control the dynamics in the active nematic film: Next, we focus on studying the dynamics of active nematics and it dependence on both the DNA linker length and binding strength. In particular, DNA linkers allow for reversible assembly of two complementary strands, wherein the size of the hybridized region controls the binding strength. Such constructs can elucidate the minimum binding energy required to generate interfilament sliding. In this vein, we assembled clusters were hybridized regions ranged from 3 base pairs (bps) to 200 bps. For lengths up to 7 bps, thermal fluctuations alone break apart a measurable fraction of clusters in experimentally relevant temperature range. Beyond this limit, within the experimental error, essentially all clusters are permanently bound (SI Appendix, Fig. S5). A hybridization length of 200 base pairs corresponds to a linker with a ~70 nm contour length. For physiological conditions the persistence length of DNA is 50 nm, so the longest linkers studied are semi-flexible filaments (46).

Depending on the binding energy, we identified three regimes of active stress generation (Fig. 3a). Clusters with a short-hybridized region (<3 bp) are not stable even in the absence of external load (SI Appendix, Fig. S5). Consequently, in this regime, most clusters attach to MTs in the monomeric (unbound) state. Thus, they are unable to generate inter-filament sliding and active stresses, and there is no discernible motor-driven dynamics. In this *weak binding* regime, the MT networks are not fluidized and do not sediment to the oil-water interface to form an active nematic (Fig. 3b).

Increasing the hybridization length increases the binding energy and the fraction of bound motors. In this *optimal binding* regime, the hybridized region ranges from 7 to 32 bps and clusters primarily bind to MTs in paired form. Such clusters generate inter-filament sliding and active stresses, which leads to a robust dynamic that is faster than the background activity due to nonspecific motor aggregation (Fig. 3b; SI Appendix, Fig. S4). Importantly, the velocity of the nematic flows increases with increasing DNA hybridization length (Fig. 3c; SI Appendix, Fig. S6). In this regime, both processive and non-processive clusters exhibit the same qualitative behavior, while showing different velocities for different hybridization lengths.

Finally, in the *stretching regime*, hybridization lengths greater than 32 bps lead to irreversibly bound clusters, even in the presence of motor generated forces. Thirty base pairs corresponds to ~10 nm; hence the linker lengths are comparable to the kinesin step size (41, 43, 44). We hypothesize that the mechanism of active stress generation in this regime occurs in multiple steps. First, the cluster binds to two MTs, typically with its DNA linker having some slack and not oriented perfectly parallel to the MTs. Second, the motors need to take one or more steps, to fully stretch and orient the DNA linker. Clusters generate MT sliding and active stresses only once its linker is fully stretched (Fig. 3a). This hypothesis is supported by the marked differences observed for clusters of processive and non-processive motors. With increasing linker length, the dynamics of nematics powered by processive clusters reached a maximum velocity for v_{dimer}~2.5 μm/s, before decreasing slightly for longest linkers studied. Processive kinesin motors move continuously over ~1 μm distances. Hence, they are able to stretch clusters with long-linkers and generate active stresses. In comparison, for non-processive clusters the active nematics speed increased with linker length, and reached a peak velocity for 16 bp linkers. Beyond 21 bp, the velocity sharply decreased. In this regime, the non-processive kinesins are unable to stretch the cluster with a single step that is a few nanometers in size, hence there is a significant reduction in interfilament sliding and active stress generation (43, 44). Intriguingly, the spatial structure of the active nematics was largely not dependent of the nature of DNA clusters (SI Appendix, Fig. S7).

Quantifying the fraction of paired force-generating motors: The above-described findings demonstrate that active stress generation requires paired clusters. Furthermore, the temporal stability of the autonomous dynamics suggests that the fraction of stress generating clusters remains constant (Fig. 1f; SI Appendix, Fig. S8). To make progress, it is essential to quantify the fraction of paired clusters. Clusters that generate active stress are paired through DNA hybridization. Thus, quantifying the amount of ds-DNA within an active nematic will yield the fraction of motors capable of generating stress. We accomplished this by using SYBR-green, a dye whose fluorescence is both linearly dependent on the ds-DNA concentration and increases by a thousand-fold upon binding to ds-DNA. Using SYBR-green we label active nematics that are powered by DNA-clusters of single-headed motors (SI Appendix, Fig S9). In comparison to double-headed clusters, the simplified structure and lower background activity of the single-headed motor allow for quantitative measurements (Fig. 3c; SI Appendix, Fig. S4) (47).

We first measured the fraction of paired clusters in equilibrium samples without molecular motors and microtubules using melting curves (Fig. 4a; SI Appendix, Fig. S5). For 7 bp linkers, ~85% of the clusters were bound. Beyond this overlap length, at room temperature, essentially all DNA was hybridized, within the measurement error. Next, using confocal imaging we quantified the SYBR-green fluorescence in an active nematic powered by single-headed kinesin motors (Fig. 4a). The fraction of paired clusters was determined by normalizing the measured signal with the signal of active nematics powered by 16 bp bound clusters that are irreversibly bound, while accounting for the differences in the hybridization lengths. In active nematics, DNA-linkers are under tension generated by molecular motors and sliding MTs. Therefore, we hypothesized that the fraction of paired clusters would be reduced in active samples when compared to quiescent solutions described above. Indeed, we found that activity significantly reduced the fraction of bound clusters. For example, for 7 bp clusters activity decreased the fraction of paired clusters from 0.85 to 0.362 ± 0.036 while for 9 bp clusters the equivalent decrease is from 1. 0 to 0.786 ± 0.063 (Fig. 4a).

Next, we verified the activity-induced decrease in the fraction of paired clusters using an independent measurement. Specifically, we compared the speed of the active nematics powered by reversible clusters that are continuously interconverting between paired and unpaired states, to samples containing a predetermined and known fraction of paired and unpaired clusters that cannot interconvert between each other. To accomplish this goal, we mixed motor clusters that are never paired (0 bp) with those that are irreversibly paired (16 bp). We then measured the active nematic speed as we changed the fraction of the two cluster types, while keeping the overall concentration constant. Measurements with these standardized samples yielded the same quantitative dependence of the velocity on the fraction of paired clusters as those obtained with the SYBR green method, thus validating the proposed method for estimating the fraction of bound clusters (Fig. 4b, c Red data set).

Quantifying cluster binding to MTs within active nematics: Quasi-2D active nematics assemble by depletion-induced adsorption of MTs from a 3D suspension onto a surfactant stabilized oil-water interface(48). While MTs are strongly adsorbed to the interface, all other components, including the motor clusters, can continuously exchange with the aqueous reservoir above the interface (Fig. 5a). Quantifying this exchange dynamics is essential for developing

models of microtubule-based active nematics. To determine the partitioning of motor clusters between the 3D reservoir and 2D active nematic, we measured the z-dependent fluorescence signal using confocal microscopy. We used 16-bp clusters, in which a fluorophore is covalently attached to the DNA linker (Fig. 5b; SI Appendix, Fig. S10). The measured signal was maximal in the nematic film, quickly decaying to a background constant value, which was ~25% of the maximum. We translate the fluorescence intensity into physical meaningful concentration units as follows. The concentration of the motors in the reservoir is 350 nM. The nematic layer thickness is estimated to be 120 nm (SI), which yields a concentration of motors in the layer of ~800 $\mathrm{clusters}/\mu\mathrm{m}^3$. From this, we estimate that there are 3 kinesin clusters (6 kinesin motors) per each microtubule (SI).

To quantify the exchange kinetics between the active nematics and the reservoir, we photo-bleached a ~20 $\mu\mathrm{m}^2$ square area in a nematic assembled at lower ATP concentrations (100 μM) and measured the fluorescence recovery (Fig. 5c). For fluorescent MTs, the bleached area remained constant, indicating an absence of significant filament exchange on the time scale of minutes (Fig. 5d). Subsequently, we bleached fluorophore-labeled motor clusters. In principle, cluster fluorescence could recover by either exchange with the 3D reservoir or by motors stepping along the MTs from the unbleached borders. For both processive and non-processive clusters the signal recovered uniformly, demonstrating that the exchange with the 3D reservoir dominates the cluster dynamics. Notably, the fluorescence of both cluster types did not recover to their original values, suggesting that a fraction of motors remained MT-bound on longer time scales (Fig. 5d; SI Appendix, Fig. S11). The fluorescence of processive motor clusters recovered to lower values compared to non-processive motors. Possible reasons include the lower exchange kinetics of such clusters are due to the effects of kinesin aggregation and formation of higher-order structures, the presence of rigor motors, and damage from photobleaching.

Fluorescence recovery curves yield the estimates of the effective rates at which motor clusters unbind from the nematic layer, k_{off}. When diffusion is faster than the molecular binding rate, the recovery of fluorescence is determined by k_{off} (49). We fit the data to an exponential curve $\propto (1 - e^{k_{\mathrm{off}} \cdot t})$ (Fig. 5e). The measured unbinding rate exhibited a weak dependence on cluster concentrations, for both processive ($k_{\mathrm{off}} \sim 0.04\ s^{-1}$) and non-processive clusters ($k_{\mathrm{off}} \sim 0.1\ s^{-1}$). A lifetime of 10 s for non-processive motors in the nematic film is significantly longer than the

duration of a single step, which is a few milliseconds. This suggests that the depletion forces and highly crowded environment within 2D active nematics induce multiple consecutive MT-kinesin stepping events before a cluster dissociates from the nematic.

Estimating the external load on DNA-motor clusters: We developed a simple model to relate the activity-induced cluster unbinding to the average load experienced by the motor clusters. A paired motor cluster is under tension due to direct forces that are exerted as its motors step along MTs. There are also indirect forces on the cluster, due to other motors that slide the MTs apart as well as the associated hydrodynamic flows. In steady-state, the fraction of bound DNA that forms clusters is determined by the balance between the DNA unbinding rate (k_{off}) with the rate of DNA binding (k_{on}). We assume that activity primarily increases k_{off} as motor generated forces shear the dsDNA that holds the cluster together. Additionally, we assume that activity-induced forces vanish for ss-DNA motor clusters; thus, k_{on} is activity-independent. With these assumptions, the fraction of unpaired clusters can be predicted by estimating the load-dependent increase of k_{off}, without the explicit knowledge of the absolute value, k_{off}. Optical tweezer measurements quantified the dependence of dsDNA rupture force on the hybridization length (50). Combining these experiments with molecular simulations provides a quantitative model of how k_{off} changes with the applied force (51). In particular, at steady-state, the force-dependent "binding constant", K, is given by the balance between on- and off-rates of the DNA:

$$K(N,f) = \frac{k_{\text{on}}}{k_{\text{off}}(N,f)} = K(N,0)e^{-\frac{(N\delta-\delta_0)f}{k_{\text{B}}T}},$$

where N is the number of base-pairs in the hybridization region, f is the applied force, δ is the extension (per base pair) of the DNA at the transition state, and δ_0 is an offset that allows for some base pairs to remain intact at the transition state.

Our model predicts how the fraction of paired clusters depends on the hybridization length and the force across the DNA linker (SI Appendix, Eq. S1-S4). With increasing force, the point where 50% of clusters are paired shifts to larger hybridization lengths (Fig. 6a). This can be quantitatively compared to the experimental measurements (Fig. 4a). As the hybridization length is experimentally controlled, the only free parameter is the applied force. The force load that yields optimal agreement with experiments is $f^* = 2.9f_{\text{stall}}$, where $f_{\text{stall}} \approx 7$ pN is a load for which the

kinesin velocity decays to zero (31). Thus, our model implies that motors operate close to or even above their stall loads. We emphasize that the above-described estimate makes simplifying assumptions. Specifically, details such as the specific sequence of the hybridized region and the ionic strength will shift the exact location of the optimal binding regime.

Relating the velocity profile to DNA-linker properties: Next, we model the dependence of the active nematics speed on the structure of the DNA linker and the motor processivity (Eq. S5). We first estimate the number of DNA clusters for which the attached motors are actively pulling pairs of neighboring microtubules (Sup Info). We assume that the force generation requires: (1) paired clusters, (2) two motors that are attached to a pair of antiparallel microtubules, and (3) alignment of clusters with the MTs so that motor-generated forces predominantly induce microtubule sliding rather than cluster reorientation. To calculate the MT sliding speeds, we use a mean field estimate of the relationship between the density of the active motors, which assumes a linear force-velocity relationship for motors (Sup info). We assume that processive motors, on average, move $l_{\mathrm{proc}} = 800$ nm before unbinding, while non-processive motors take a single 8 nm step. Motivated by the possibility that an effective processivity arises due to depletant-induced attractions between the motor constructs and microtubules, we have also considered an intermediate processivity length of 10 steps.

The calculated interfilament sliding velocity as a function of DNA linker length and motor processivity (Fig. 6b) exhibits similar trends as the experimental observations (Fig. 3c). Note that the magnitude of the measured speeds differs by orders of magnitude. Our model predicts the relative sliding speed of two neighboring filaments. The filaments are extending everywhere within the active nematics. The mechanisms by which these local extension generate much faster large-scale dynamics are described elsewhere (52). The predicted decrease in velocity with hybridization for low processivity clusters is more gradual in our model when compared to experimental observations. A possible reason is the assumption that the rate of motor construct reorientation is limited only by the kinesin stepping rate, whereas motor construct motions could be impeded by the dense environment of the active nematic.

Discussion: Active nematics are powered by kinesin clusters that simultaneously bind to two antiparallel MTs. However, the microscopic details of how motors power interfilament sliding are

unknown. We demonstrated that single-headed non-processive motors power active nematics as efficiently as processive motors. Furthermore, our analysis reveals that the force load on single-headed motor clusters is ~20 pN, which is significantly larger than the 7 pN stall force that has been measured for processive motors. At first, these findings might appear inconsistent with the efficient generation of interfilament sliding, which requires that both motors are simultaneously engaged with two MT filaments. Analysis of conventional motility assays powered by single-headed kinesins suggests that motors are engaged with a MT at most ~50% of the time (44). Thus, the probability of both motors being simultaneously engaged with MTs seems small. Naively one would expect that the external load would enhance the motor unbinding and thus further reduce the efficiency of interfilament sliding. However, recent studies demonstrated that the kinesin-MT unbind rate is highly dependent on both the direction and the magnitude of the external load, suggesting a possible mechanism that resolves above-described inconsistencies (53, 54). In particular, resisting loads applied along the MTs long axis significantly *decrease* the kinesin-MT unbinding rate. For example, a ~20 pN resisting load increases the kinesin-filament bond lifetime by multiple orders of magnitude when compared to load-free conditions. In comparison, forces perpendicular to the MTs long axis decrease the bond lifetime. Thus, for certain conditions, kinesin forms a catch bond whose strength increases with the applied load.

In active nematics, the two motors are coupled via a linker, which ensures that they experience resisting loads. Furthermore, the nematic alignment of clusters demonstrates that the resistive loads primarily point along the MTs long axis, a direction that maximally increases the lifetime of the MT-kinesin bond. Thus, load-dependent unbinding might be essential for the efficient generation of interfilament sliding. Large loads increase the bond lifetime, which greatly increases the efficiency of clusters crosslinking two filaments and inducing their relative sliding.

Two types of events could drive cluster rupture. The clusters could rupture due to forces applied by the motors during their power stroke. Alternatively, the clusters could rupture while passively linking a filament pair whose relative sliding motion is powered by other motors. The direct force produced by a motor construct occurs primarily during the power stroke of each kinesin, which has a ~10 μs time scale. This is a small fraction of the entire hydrolysis cycle, which at saturating ATP lasts ~10 ms (31). The probability of bond rupture depends on both the magnitude of the applied force and the time scale over which this force is applied (55). Because of its short duration,

forces acting during the power stroke alone would have to be orders of magnitude larger to induce unbinding of a significant fraction of clusters. Instead, our results are consistent with cluster unbinding induced by forces that are on the order of, or larger than, the stall force, and are applied over a large fraction of the motor hydrolysis lifetime. Thus, forces experienced by the motor constructs arise primarily due to microtubule motions induced by other motors within the nematic.

In the conventional view, MT-based active nematics are viscous fluids in which motor clusters step along two microtubules, generating interfilament sliding that drives large-scale chaotic motion. Intriguingly, recent experiments visualizing single filament dynamics suggest that interfilament sliding in a dense nematic is not easily connected to the sliding of individual microtubule (52). The results described here suggest an alternative scenario. On average, there are 6 kinesin motors interacting with each filament, with each motor applying a ~20 pN force for the majority of its lifetime. Each cluster likely links different MT pairs. Thus MT-based liquid crystals are heavily crosslinked structures similar to previously studied gels linked with kinesin-14 motors (28). Individual motors attached to any given MT push in opposite directions. Thus, forces on a MT are mostly balanced, which gives rise to large pre-stress, as has been measured in actomyosin gels (56). In such materials, MT motion would arise from fluctuations in the net force. Multiple microscopic events could cause unbalance in the net force: (1) a motor might take a power stroke that increases the DNA linker tension, (2) a motor could unbind and release the tension, or (3) the DNA-linker could rupture. These results demonstrate the need to develop novel rheological techniques capable of characterizing 2D active nematics. Furthermore, having an estimate of load on each linker reveals that the average stresses exerted by the motors in the gel are ~1-40 kPa (SI).

In summary, we developed a programmable kinesin motor cluster capable of driving MT-based active nematics. The unique capabilities of the developed system provide new insight into possible mechanisms by which nanometer-sized kinesin motors drive macroscale chaotic flows. More broadly, our system illustrates potential synergies that arise by merging the precision of the DNA nanotechnology with the emerging field of active matter.

Methods

Tubulin purification and microtubules polymerization: Tubulin was purified from bovine brain through 2 cycles of polymerization and depolymerization (57). Tubulin was stored at -80° C and subsequently recycled through an additional polymerization and depolymerization step. For fluorescent imaging, tubulin was labeled with Alex-647 dye (Invitrogen, A-20006) using a succinimidyl ester linker (58, 59). Absorbance spectrum showed that the percentage of labeled tubulin was 30-60%. Microtubules (MTs) were polymerized from a mixture of recycled tubulin and 4% labeled monomers in a buffer containing 10 mM GMPCPP (Jena Biosciences), 20 mM DTT in M2B (80 mM PIPES, pH 7, 1 mM EGTA, 2 mM MgCl2). The final tubulin concentration was 8 mg/ml. The suspension was incubated at 35°C for 30 min, allowed to sit at room temperature for 5 hours, flash frozen in liquid nitrogen, and stored at -80° C.

Kinesin purification: Kinesin-401(dimeric kinesin) and kinesin-365 (monomeric kinesin) consist of 401 and 365 amino acids of the N-terminal motor domain of *D. melanogaster* kinesin. Both motors were cloned with fusion to the SNAP tag, and purified as previously published (60). The SNAP-tag is appended to the cargo binding region of the motor. The protein was flash frozen in liquid nitrogen and stored at -80° C.

DNA-BG labeling: 5'-amine modified DNA oligos (IDT) were labeled with BG-GLA-NHS (NEB) (40, 61). Briefly, oligos at 2 mM concentration were mixed with BG-GLA-NHS (15-20 mM in DMSO) in HEPES buffer (200 mM, PH 8.4) at a volume ratio of 1:2:3. BG-GLA-NHS was added last to the mixture. The mixture was incubated for 30 min at room temp. DNA was separated from excess BG using size exclusion spin column (Micro Bio-Spin 6 columns, Bio-Rad). Prior to DNA cleaning, tris-buffer in the column was exchanged with PBS (PH 7.2) according to manufacturer instructions. The separation step was repeated 4 times. The labeling efficiency, between 70-100%, was determined by DNA gel electrophoresis (20% TBE acrylamide gel for 60 min at 200 V). Labelled DNA oligos were stored at -20° C.

Assembly of DNA-motor clusters: DNA oligos were annealed to their complementary strands. DNA mixture in a duplex buffer (100 mM Potassium Acetate; 30 mM HEPES, pH 7.5) was heated to 95° C for 10 min, and gradually cooled down to room temperature in a heat block left on the bench. Annealed DNA were either stored at -20° C or used immediately. ds-DNA with BG-modified 5' ends was mixed with SNAP-tagged kinesin motors at a molar ratio of 2:1 (kinesin:DNA). The DNA-kinesin mixture was incubated for 30 min at room temperature prior to

the experiment. Dimeric kinesin has two heads for each DNA, whereas monomeric kinesin has one head. The formation of motor clusters was verified using gel electrophoresis, revealing that ~70-80% of the DNA was labeled with the kinesin, for both monomeric and dimeric kinesin (SI Appendix, Fig. S1).

MT-based active nematic: Active nematics were assembled as described previously (62, 63). The only difference involved the assembly of flow chamber with rain-X treated coverslip instead of Aquapel.

Visualizing DNA active nematics: In experiments requiring visualization of DNA, MTs were not labeled to prevent signal blead-through. DNA was labeled with YOYO-1 (Fisher Scientific) at a concentration of 100-200 nM, or SYBR green at a dilution of 1:5000. For measuring *z*-profiles, DNA clusters were labeled internally with either Cy3 or Cy5 fluorophore.

Active nematics were imaged using conventional fluorescence microscopy using Nikon Ti-2 and an Andor-Zyla camera running open-source microscopy managing software Micro-Manager 1.4.23. DNA intercalators were imaged using scanning laser Leica-SP8 confocal microscope. To suppress light inhomogeneity throughout the sample and minimize signal from different z-sections, the polarization anisotropy imaging was conducted with a Leica-SP8 confocal microscope. A polarizer in the light path that served both as a polarizer and analyzer. Photobleaching recovery experiments were conducted on the SP8-Leica confocal with a 20x NA 0.75 objective and a 488 nm laser source at 40X zoom. Velocity measurements were conducted by particle tracking (Alexa-488 labeled silica beads 3 μm diameter) or with the MatLab PIV tool.

References

1. M. C. Marchetti, *et al.*, Hydrodynamics of soft active matter. *Rev. Mod. Phys.* **85**, 1143–1189 (2013).
2. I. Theurkauff, C. Cottin-Bizonne, J. Palacci, C. Ybert, L. Bocquet, Dynamic clustering in active colloidal suspensions with chemical signaling. *Phys. Rev. Lett.* **108**, 268303–268303 (2012).
3. J. Palacci, S. Sacanna, A. P. Steinberg, D. J. Pine, P. M. Chaikin, Living Crystals of Light-Activated Colloidal Surfers. *Science.* **339**, 936–940 (2013).
4. G. S. Redner, M. F. Hagan, A. Baskaran, Structure and Dynamics of a Phase-Separating Active Colloidal Fluid. *Phys. Rev. Lett.* **110**, 055701 (2013).

5. Y. Fily, M. C. Marchetti, Athermal phase separation of self-propelled particles with no alignment. *Phys. Rev. Lett.* **108**, 235702–235702 (2012).
6. J. Brugués, D. Needleman, Physical basis of spindle self-organization. *Proc. Natl. Acad. Sci. U. S. A.* **111**, 18496–18500 (2014).
7. R. Aditi Simha, S. Ramaswamy, Hydrodynamic fluctuations and instabilities in ordered suspensions of self-propelled particles. *Phys. Rev. Lett.* **89**, 058101 (2002).
8. D. Saintillan, M. J. Shelley, Hydrodynamic fluctuations and instabilities in ordered suspensions of self-propelled particles. *Phys. Fluids* **20**, 123304 (2008).
9. V. Narayan, S. Ramaswamy, N. Menon, Long-lived giant number fluctuations in a swarming granular nematic. *Science.* **317**, 105–108 (2007).
10. K. Kawaguchi, R. Kageyama, M. Sano, Topological defects control collective dynamics in neural progenitor cell cultures. *Nature* **545**, 327–331 (2017).
11. S. Zhou, A. Sokolov, O. D. Lavrentovich, I. S. Aranson, Living liquid crystals. *Proc. Natl. Acad. Sci. U. S. A.* **111**, 1265–1270 (2014).
12. L. Giomi, M. J. Bowick, X. Ma, M. C. Marchetti, Defect Annihilation and Proliferation in Active Nematics. *Phys. Rev. Lett.* **110**, 228101 (2013).
13. S. P. Thampi, R. Golestanian, J. M. Yeomans, Instabilities and topological defects in active nematics. *EPL* **105**, 18001 (2014).
14. H. H. Wensink, *et al.*, Meso-scale turbulence in living fluids. *Proc. Natl. Acad. Sci.* **109**, 14308–14313 (2012).
15. X. Shi, Y. Ma, Topological structure dynamics revealing collective evolution in active nematics. *Nat. Commun.* **4**, 3013 (2013).
16. E. Putzig, G. S. Redner, A. Baskaran, A. Baskaran, Instabilities, defects, and defect ordering in an overdamped active nematic. *Soft Matter* **12**, 3854–3859 (2016).
17. T. Sanchez, D. T. N. Chen, S. J. DeCamp, M. Heymann, Z. Dogic, Spontaneous motion in hierarchically assembled active matter. *Nature* **491**, 431–434 (2012).
18. N. Kumar, R. Zhang, J. J. De Pablo, M. L. Gardel, Tunable structure and dynamics of active liquid crystals. *Sci. Adv.* **4**, eaat7779 (2018).
19. P. Guillamat, J. Ignés-Mullol, F. Sagués, Control of active liquid crystals with a magnetic field. *Proc. Natl. Acad. Sci. U. S. A.* **113**, 5498–5502 (2016).
20. K.-T. Wu, *et al.*, Transition from turbulent to coherent flows in confined three-

dimensional active fluids. *Science.* **355** (2017).

21. P. W. Ellis, *et al.*, Curvature-induced defect unbinding and dynamics in active nematic toroids. *Nat. Phys.* **14**, 85–90 (2018).
22. A. J. Tan, *et al.*, Topological chaos in active nematics. *Nat. Phys.* **15**, 1033–1039 (2019).
23. A. Opathalage, *et al.*, Self-organized dynamics and the transition to turbulence of confined active nematics. *Proc. Natl. Acad. Sci. U. S. A.* **116**, 4788–4797 (2019).
24. M. Varghese, A. Baskaran, M. F. Hagan, A. Baskaran, Confinement-Induced Self-Pumping in 3D Active Fluids. *Phys. Rev. Lett.* **125**, 268003 (2020).
25. M. Ravnik, J. M. Yeomans, Confined Active Nematic Flow in Cylindrical Capillaries. *Phys. Rev. Lett.* **110**, 026001 (2013).
26. P. Chandrakar, *et al.*, Confinement Controls the Bend Instability of Three-Dimensional Active Liquid Crystals. *Phys. Rev. Lett.* **125**, 257801 (2020).
27. T. Gao, R. Blackwell, M. A. Glaser, M. D. Betterton, M. J. Shelley, Multiscale Polar Theory of Microtubule and Motor-Protein Assemblies. *Phys. Rev. Lett.* **114**, 048101 (2015).
28. S. Fürthauer, *et al.*, Self-straining of actively crosslinked microtubule networks. *Nat. Phys.* **15**, 1295–1300 (2019).
29. D. Needleman, Z. Dogic, Active matter at the interface between materials science and cell biology. *Nat. Rev. Mater.* **2**, 1–14 (2017).
30. A. Yildiz, M. Tomishige, R. D. Vale, P. R. Selvin, Kinesin Walks Hand-Over-Hand. *Science.* **303**, 676–678 (2004).
31. K. Visscher, M. J. Schnltzer, S. M. Block, Single kinesin molecules studied with a molecular force clamp. *Nature* **400**, 184–189 (1999).
32. K. C. Neuman, A. Nagy, Single-molecule force spectroscopy: optical tweezers, magnetic tweezers and atomic force microscopy. *Nat. Methods* **5**, 491–505 (2008).
33. P. C. Nickels, *et al.*, Molecular force spectroscopy with a DNA origami-based nanoscopic force clamp. *Science.* **354**, 305–307 (2016).
34. X. Wang, T. Ha, Defining single molecular forces required to activate integrin and Notch signaling. *Science.* **340**, 991–994 (2013).
35. A. T. Blanchard, K. Salaita, Emerging uses of DNA mechanical devices. *Science.* **365**, 1080–1081 (2019).

36. H. Shroff, *et al.*, Biocompatible Force Sensor with Optical Readout and Dimensions of 6 nm 3. *Nano Lett.* **5**, 1509–1514 (2005).
37. J. M. Brockman, *et al.*, Mapping the 3D orientation of piconewton integrin traction forces. *Nat. Methods* **15**, 115–118 (2018).
38. T. D. Ross, *et al.*, Controlling organization and forces in active matter through optically defined boundaries. *Nature* **572**, 224–229 (2019).
39. F. J. Nédélec, T. Surrey, A. C. Maggs, S. Leibler, Self-organization of microtubules and motors. *Nature* **389**, 305–308 (1997).
40. N. D. Derr, *et al.*, Tug-of-war in motor protein ensembles revealed with a programmable DNA origami scaffold. *Science.* **338**, 662–665 (2012).
41. A. Yildiz, M. Tomishige, R. D. Vale, P. R. Selvin, Kinesin Walks Hand-Over-Hand. *Science.* **303**, 676–678 (2004).
42. E. Berliner, E. C. Young, K. Anderson, H. K. Mahtani, J. Gelles, Failure of a single-headed kinesin to track parallel to microtubule protofilaments. *Nature* **373**, 718–721 (1995).
43. W. O. Hancock, J. Howard, Processivity of the motor protein kinesin requires two heads. *J. Cell Biol.* **140**, 1395–1405 (1998).
44. E. C. Young, H. K. Mahtani, J. Gelles, One-headed kinesin derivatives move by a nonprocessive, low-duty ratio mechanism unlike that of two-headed kinesin. *Biochemistry* **37**, 3467–3479 (1998).
45. A. S. Backer, *et al.*, Single-molecule polarization microscopy of DNA intercalators sheds light on the structure of S-DNA. *Sci. Adv.* **5**, eaav1083 (2019).
46. C. G. Baumann, S. B. Smith, V. A. Bloomfield, C. Bustamante, Ionic effects on the elasticity of single DNA molecules. *Proc. Natl. Acad. Sci. U. S. A.* **94**, 6185–6190 (1997).
47. J. Mackay, O. Landt, Real-time PCR fluorescent chemistries. *Methods Mol. Biol.* **353**, 237–261 (2007).
48. D. Welch, M. P. Lettinga, M. Ripoll, Z. Dogic, G. A. Vliegenthart, Trains, tails and loops of partially adsorbed semi-flexible filaments. *Soft Matter* **11**, 7507–7514 (2015).
49. B. L. Sprague, R. L. Pego, D. A. Stavreva, J. G. McNally, Analysis of Binding Reactions by Fluorescence Recovery after Photobleaching. *Biophys. J.* **86**, 3473–3495 (2004).
50. K. Hatch, C. Danilowicz, V. Coljee, M. Prentiss, Demonstration that the shear force

required to separate short double-stranded DNA does not increase significantly with sequence length for sequences longer than 25 base pairs. *Phys. Rev. E - Stat. Nonlinear, Soft Matter Phys.* **78**, 011920 (2008).

51. M. Mosayebi, A. A. Louis, J. P. K. Doye, T. E. Ouldridge, Force-Induced Rupture of a DNA Duplex: From Fundamentals to Force Sensors. *ACS Nano* **9**, 11993–12003 (2015).
52. L. M. Lemma, *et al.*, Multiscale Dynamics in Active Nematics (2020) (July 20, 2020).
53. J. O. L. Andreasson, *et al.*, Examining kinesin processivity within a general gating framework. *Elife* **2015**, 1–44 (2015).
54. H. Khataee, J. Howard, Force Generated by Two Kinesin Motors Depends on the Load Direction and Intermolecular Coupling. *Phys. Rev. Lett.* **122**, 188101 (2019).
55. R. Merkel, P. Nassoy, A. Leung, K. Ritchie, E. Evans, Energy landscapes of receptor–ligand bonds explored with dynamic force spectroscopy. *Nature* **397**, 50–53 (1999).
56. G. H. Koenderink, *et al.*, An active biopolymer network controlled by molecular motors. *Proc. Natl. Acad. Sci.* **106**, 15192–15197 (2009).
57. M. Castoldi, A. V. Popov, Purification of brain tubulin through two cycles of polymerization- depolymerization in a high-molarity buffer. *Protein Expr. Purif.* **32**, 83–88 (2003).
58. T. Sanchez, D. Welch, D. Nicastro, Z. Dogic, Cilia-like beating of active microtubule bundles. *Science* **333**, 456–9 (2011).
59. G. Henkin, S. J. DeCamp, D. T. N. Chen, T. Sanchez, Z. Dogic, Tunable dynamics of microtubule-based active isotropic gels. *Philos. Trans. R. Soc. A Math. Phys. Eng. Sci.* **372**, 20140142 (2014).
60. E. C. Young, E. Berliner, H. K. Mahtani, B. Perez-Ramirez, J. Gelles, Subunit interactions in dimeric kinesin heavy chain derivatives that lack the kinesin rod. *J. Biol. Chem.* **270**, 3926–3931 (1995).
61. B. S. Goodman, S. L. Reck-Peterson, "Engineering defined motor ensembles with DNA origami" in *Methods in Enzymology*, (Academic Press Inc., 2014), pp. 169–188.
62. F. C. Keber, *et al.*, Topology and dynamics of active nematic vesicles. *Science* **345**, 1135–9 (2014).
63. S. J. DeCamp, G. S. Redner, A. Baskaran, M. F. Hagan, Z. Dogic, Orientational order of motile defects in active nematics. *Nat. Mater.* **14**, 1110–1115 (2015).

* This manuscript was primarily supported by the Department of Energy, Basic Energy Sciences through award DE-SC0019733. Development of the theoretical model was supported by NSF DMR-1855914 and the Brandeis Center for Bioinspired Soft Materials, an NSF-MRSEC (DMR-2011846). We also acknowledge use of the Brandeis MRSEC BioSynthesis Facility which is supported by DMR-2011846. Alexandra M. Tayar is a Simons Foundation Fellow of the Life Sciences Research Foundation and is an Awardee of the Weizmann Institute of Science -National Postdoctoral Award Program for Advancing Women in Science. We also acknowledge the KITP Active20 program, which is supported in part by the National Science Foundation under Grant No. NSF PHY-1748958. Illustrations were created with BioRender.com

Figure captions

Fig. 1- Active nematics powered by DNA-kinesin clusters. (a) Schematic of a DNA motor cluster. Processive (double-headed) and non-processive (single-headed) kinesin motors bind to the dsDNA's end by a SNAP-BG covalent bond. The DNA is internally labeled with a fluorophore. The hybridization length controls the cluster binding strength. Double-headed kinesins moves processively on MTs for ~100 consecutive steps. Single-headed kinesins unbind from MTs after each step. **(b)** Schematic of a kinesin-MT bundle, the elemental structural motif that exerts extensile stresses and drives the active nematic. MTs are bundled by the depletion agent PEG, and motor clusters crosslink the filaments and induce their sliding. Bundles are confined to a surfactant-stabilized oil-water interface, where they form a dense 2D nematic film. **(c)** Fluorescence image of a 2D active nematic film, microtubules labeled; arrows indicate local velocity magnitude and direction. **(d)** Active nematic composed of fluorescent microtubules. **(e)** Active nematic containing unlabeled MTs but fluorescently labelled DNA clusters. Scale bar, 100 μm. **(f)** Spatially average velocity of autonomous flows of an active nematic film showing stability over time. The velocity is measured from micron-sized passive tracer particles embedded in the layer averaged over space.

Fig. 2 - Orientational order of DNA clusters (a) Schematic of a DNA motor cluster labeled with an intercalator dye orientation between two MTs. Polarized light excites the intercalated dyes, and the emitted fluorescence is measured using a colinear analyzer. Orientation of intercalating dye dipoles indicated with bidirectional arrows; the dye molecules are at 90^0 to the DNA long axis. ϕ is the angle between the DNA long axis and the polarizer/analyzer (P/A) axis. θ is the standard deviation of the DNA orientational distribution. **(b)** Fluorescence anisotropy of active nematics. Bidirectional arrows indicate P/A orientations. White lines correspond to director field. Emitted fluorescence is maximum when dye points along the P/A axis. **(c)** Normalized fluorescence intensity as a function of ϕ for 3 different cluster types: 100 bp double-headed clusters, 15 bp double-headed clusters, and 15 bp single-headed clusters. Maximal intensity at $\phi = 90^0$ indicates that the DNA is aligned with the MTs. Error bars are standard errors averaged over n = 20-100 events in a measured angle. Lines are fit to a model assuming a normal distribution of angles ϕ. The values of θ are estimated by least square method minimizing χ^2, the errors are estimated by

increasing χ^2 in 1 from the minimum value, giving a variation of one standard deviation in θ. Inset: probability distribution, $p(\phi)$ for the three different cluster types.

Figure 3- Cluster binding energy controls active stress. (a) Changing the DNA motor cluster hybridization length reveals different regimes of active stress generation. *Weak binding:* for short hybridization lengths (< 6 bp), the cluster binding energy is a few k_BT; hence clusters are unable to generate interfilament sliding. *Optimal binding:* for intermediate hybridization length 7-21bp, the strong cluster binding energy enable motor drive interfilament sliding. *DNA stretching:* for long hybridization lengths (> 21 bp) processive motors take multiple steps to stretch the DNA and then generate interfilament sliding. Single-headed clusters are unable to stretch the linker in a single step; thus, they generate no sliding. **(b)** An active nematic in the optimal binding regime (16 bp), and an isotropic static network formed in the weak binding regime for a single headed motor (3 bp). **(c)** Average speed of active nematic flows as a function of the linker hybridization length, for both processive (blue) and non-processive (orange) clusters. Velocities are measured from tracking 3 μm beads embedded in the nematic. Error bars are standard errors over N=4-8 measurements.

Figure 4- Quantifying the fraction of paired motor clusters. (a) Fraction of bound clusters as a function of DNA hybridization length in active nematics (red dots) and equilibrium suspensions (blue dots). Error bars are standard errors over 8-10 samples. **(b)** Speed of active nematic flows as a function of hybridization length. **(c)** Active nematic speed as a function of fraction of paired clusters (black points). The fraction of bound motors was controlled by changing DNA hybridization length; the data is taken from the y-axis value of the red data points in panels a and b. (red points) Control experiments where the fraction of paired and unpaired clusters was determined by changing the ratio of 16 and 0 hybridization length linkers. Error bars are standard errors over 6-8 samples.

Figure 5- Binding of motor clusters to 2D active nematics. (a) 2D active nematic assembled on a surfactant-stabilized oil-water interface. Clusters partition between 2D nematics and the 3D reservoir located on the aqueous side of the interface. **(b)** Z-dependent fluorescence intensity profiles of the motor clusters. The nematic is located at z=0. For additional profiles see SI Appendix Fig. S10. **(c)** Fluorescence recovery after photobleaching (FRAP) images of fluorescently labeled MTs, processive, and non-processive motor clusters. DNA motor clusters are covalently labeled. **(d)** Spatial profile along the bleached window for MTs, processive, and non-processive motor clusters. **(e) A** Temporal profile of the fluorescence recovery after bleaching. Lines are fits to: $a \cdot (1 - be^{-k_{\text{off}} \cdot t})$. For additional profiles see SI Appendix Fig. S11. **(f)** k_{off} for processive and non-processive motor clusters. Errors are the standard deviation (n=4). FRAP experiments were conducted at $[ATP] = 100$ μM to slow the system dynamics.

Fig. 6- Force load determines the fraction of paired clusters. (a) Fraction of hybridized dimers as a function of hybridization length in equilibrium and under different force loads. Experimental data is indicated by circles. The best fit to experimental data is obtained for $f = 2.91\ f_{\text{stall}}$, where $f_{\text{stall}} = 7$ pN. **(b)** Relative velocity between MT pairs predicted as a function of base pair overlap

for processivity lengths corresponding to 1, 10, and 100 steps, with a step length of 8 nm. Error bars are standard error over 3-4 measurements.

Figures

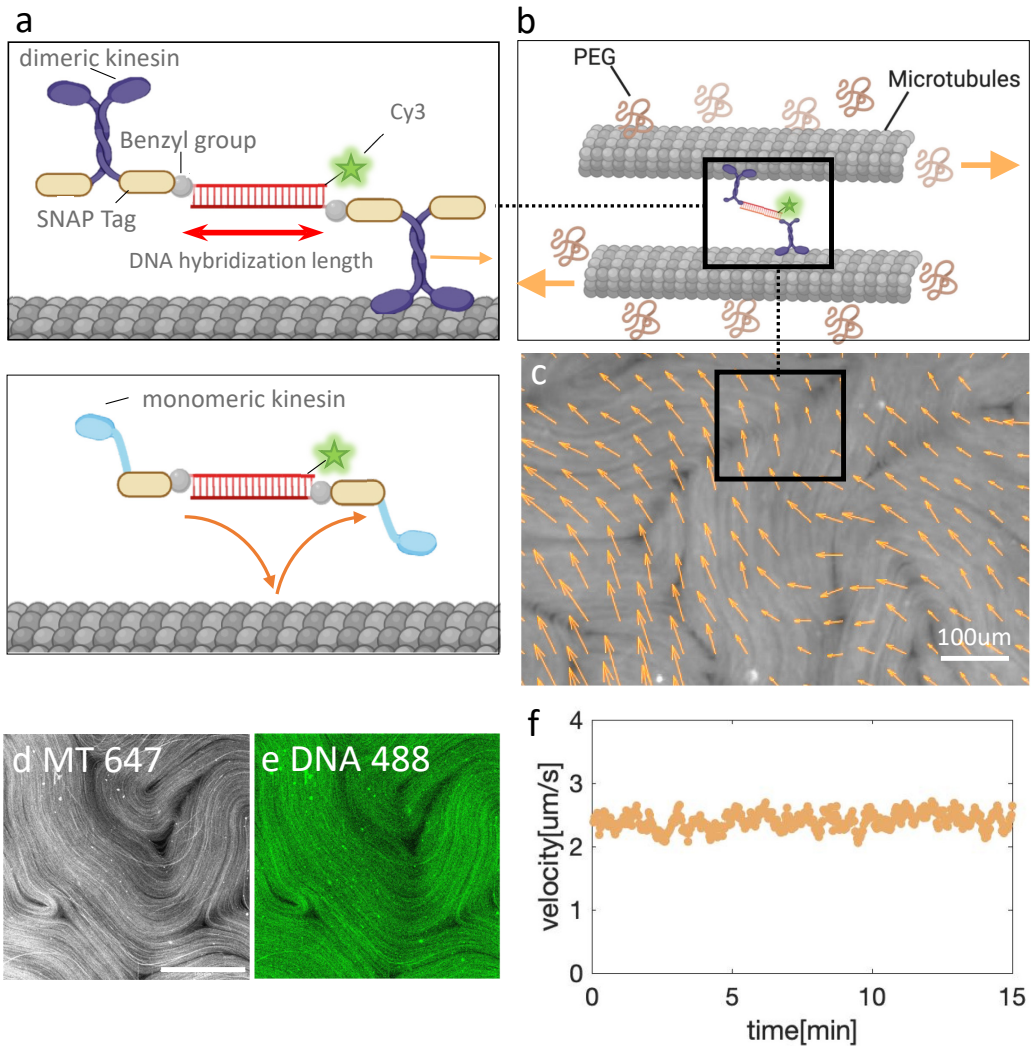

Fig. 1

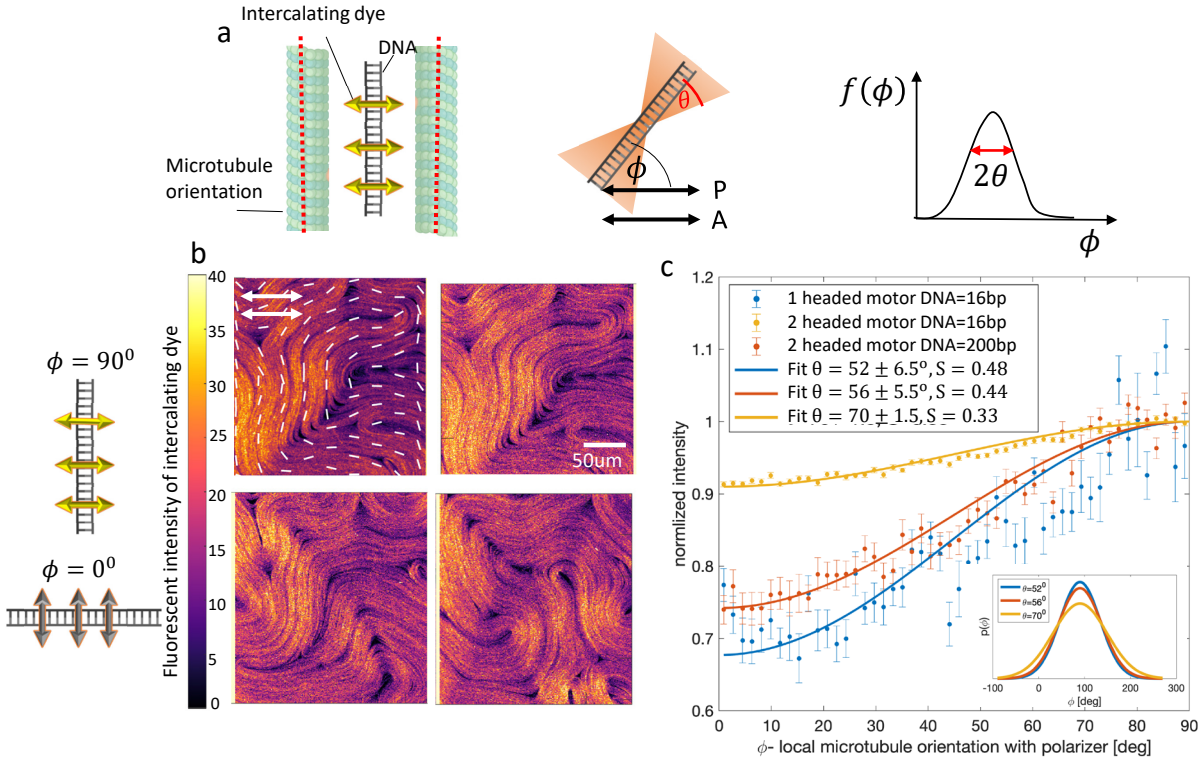
a
Intercalating dye
DNA
Microtubule orientation
θ
ϕ
P
A
$f(\phi)$
2θ
ϕ
b
$\phi = 90^0$
$\phi = 0^0$
Fluorescent intensity of intercalating dye
40
35
30
25
20
15
10
5
0
50um
c
1 headed motor DNA=16bp
2 headed motor DNA=16bp
2 headed motor DNA=200bp
Fit θ = 52 ± 6.5°, S = 0.48
Fit θ = 56 ± 5.5°, S = 0.44
Fit θ = 70 ± 1.5, S = 0.33
normlized intensity
1.2
1.1
1
0.9
0.8
0.7
0.6
0
10
20
30
40
50
60
70
80
90
ϕ- local microtubule orientation with polarizer [deg]
p(ϕ)
θ=52°
θ=56°
θ=70°
-100
0
100
200
300
ϕ [deg]

Fig. 2

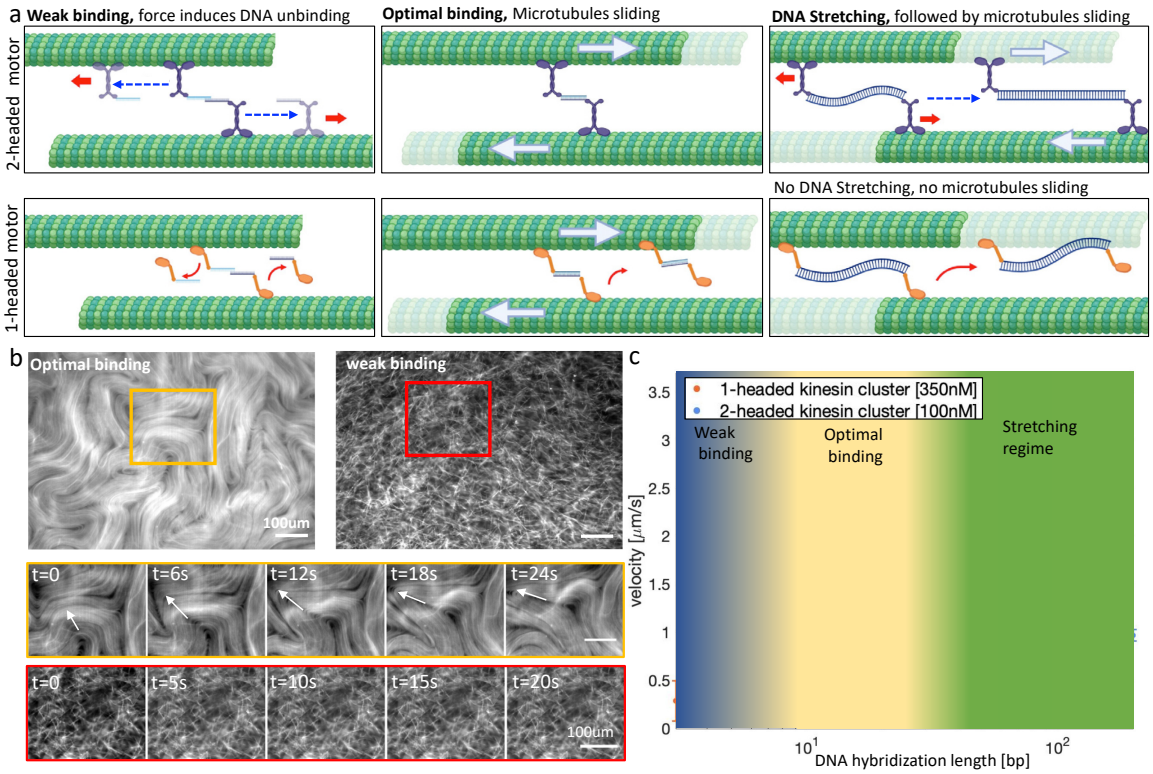
a
Weak binding, force induces DNA unbinding
Optimal binding, Microtubules sliding
DNA Stretching, followed by microtubules sliding
2-headed motor
1-headed motor
No DNA Stretching, no microtubules sliding
b
Optimal binding
weak binding
100um
t=0
t=6s
t=12s
t=18s
t=24s
t=0
t=5s
t=10s
t=15s
t=20s
100um
c
1-headed kinesin cluster [350nM]
2-headed kinesin cluster [100nM]
Weak binding
Optimal binding
Stretching regime
velocity [μm/s]
DNA hybridization length [bp]

Fig. 3

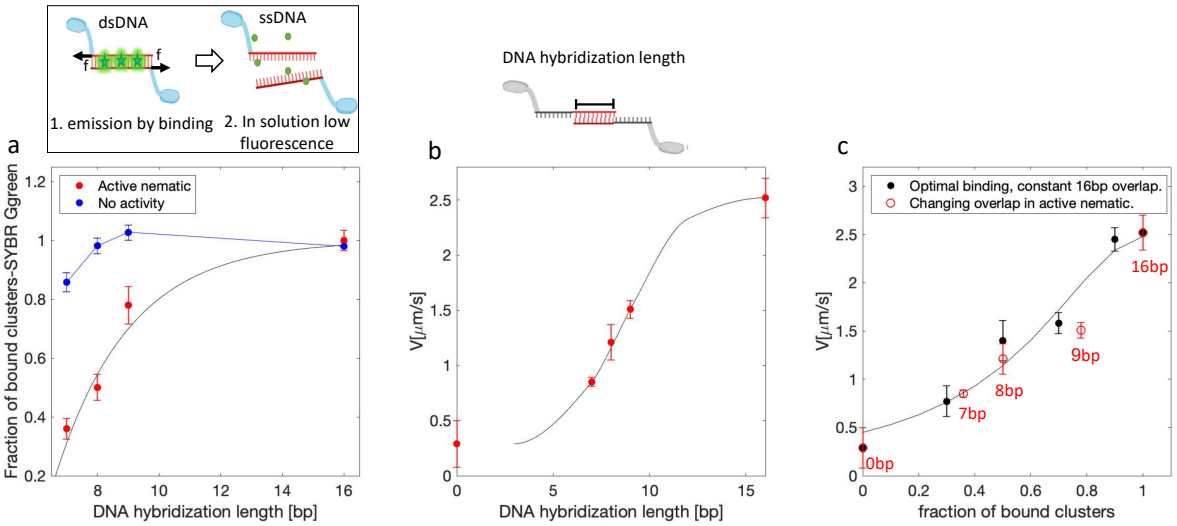
dsDNA
ssDNA
f
1. emission by binding
2. In solution low fluorescence
a
Active nematic
No activity
Fraction of bound clusters-SYBR Ggreen
DNA hybridization length [bp]
DNA hybridization length
b
V[μm/s]
DNA hybridization length [bp]
c
Optimal binding, constant 16bp overlap.
Changing overlap in active nematic.
V[μm/s]
fraction of bound clusters
0bp
7bp
8bp
9bp
16bp

Fig. 4

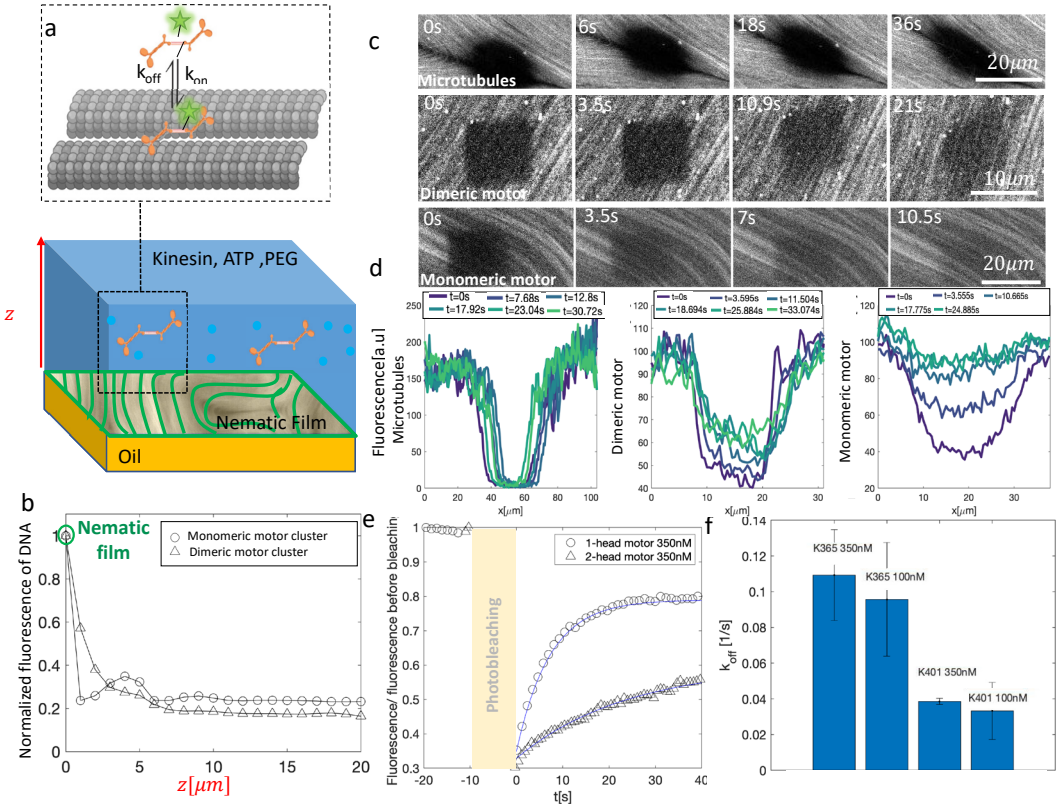
a
k_{off}
k_{on}
Kinesin, ATP ,PEG
z
Nematic Film
Oil
b
Nematic film
Monomeric motor cluster
Dimeric motor cluster
Normalized fluorescence of DNA
$z[\mu m]$
c
0s
6s
18s
36s
20μm
Microtubules
0s
3.5s
10.9s
21s
10μm
Dimeric motor
0s
3.5s
7s
10.5s
20μm
Monomeric motor
d
Fluorescence[a.u]
Microtubules
Dimeric motor
Monomeric motor
x[μm]
e
1-head motor 350nM
2-head motor 350nM
Photobleaching
Fluorescence/ fluorescence before bleachin
t[s]
f
K365 350nM
K365 100nM
K401 350nM
K401 100nM
k_{off} [1/s]

Fig. 5

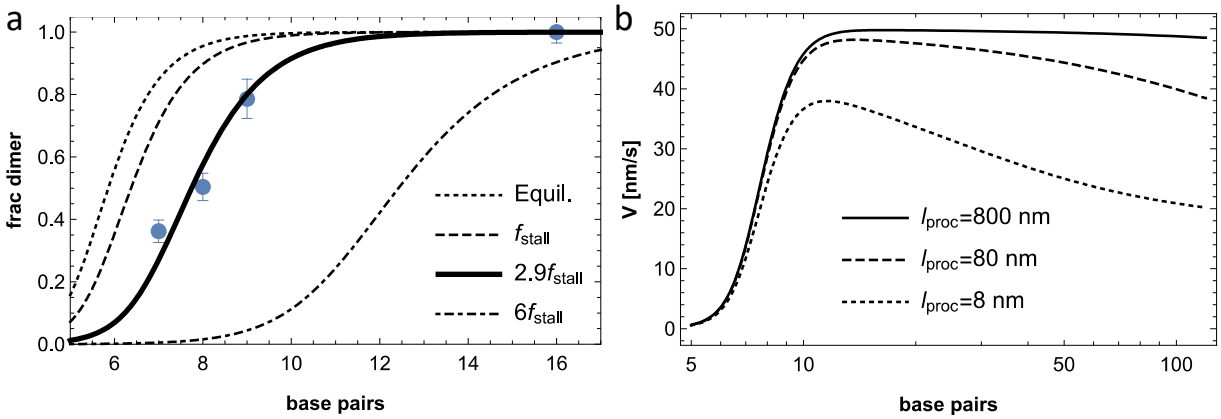
a
frac dimer
base pairs
Equil.
f_{stall}
$2.9f_{stall}$
$6f_{stall}$
b
V [nm/s]
base pairs
l_{proc}=800 nm
l_{proc}=80 nm
l_{proc}=8 nm

Fig. 6